Strain tuning of nematicity and superconductivity in single crystals of FeSe

Michele Ghini [1,2,*] Matthew Bristow [1] Joseph C. A. Prentice [3] Samuel Sutherland,[1] Samuele Sanna [2]
A. A. Haghighirad [1,4] and A. I. Coldea [1,†]

[1]*Clarendon Laboratory, Department of Physics, University of Oxford, Parks Road, Oxford OX1 3PU, United Kingdom*
[2]*Department of Physics and Astronomy, A. Righi, University of Bologna, via Berti Pichat 6-2, I-40127 Bologna, Italy*
[3]*Department of Materials, University of Oxford, Parks Road, Oxford OX1 3PH, United Kingdom*
[4]*Institute for Quantum Materials and Technologies (IQMT), Karlsruhe Institute of Technology, 76021 Karlsruhe, Germany*

Strain is a powerful experimental tool to explore new electronic states and understand unconventional super-conductivity. Here, we investigate the effect of uniaxial strain on the nematic and superconducting phase of single crystal FeSe using magnetotransport measurements. We find that the resistivity response to the strain is strongly temperature dependent and it correlates with the sign change in the Hall coefficient being driven by scattering, coupling with the lattice and multiband phenomena. Band-structure calculations suggest that under strain the electron pockets develop a large in-plane anisotropy as compared with the hole pocket. Magnetotransport studies at low temperatures indicate that the mobility of the dominant carriers increases with tensile strain. Close to the critical temperature, all resistivity curves at constant strain cross in a single point, indicating a universal critical exponent linked to a strain-induced phase transition. Our results indicate that the superconducting state is enhanced under compressive strain and suppressed under tensile strain, in agreement with the trends observed in FeSe thin films and overdoped pnictides, whereas the nematic phase seems to be affected in the opposite way by the uniaxial strain. By comparing the enhanced superconductivity under strain of different systems, our results suggest that strain on its own cannot account for the enhanced high T_c superconductivity of FeSe systems.

I. INTRODUCTION

Uniaxial strain can considerably alter unconventional su-perconductivity [1–3] or nematic and magnetic phases in iron-based superconductors [4,5], demonstrating that it is a powerful tool to induce phase transitions and explore the in-terplay of different competing phases with superconductivity. A nematic phase is an electronic state of matter in which the electronic structure develops strong in-plane anisotropy in transport properties, breaking the rotational symmetry of the tetragonal lattice. Strain is also used as a small perturbation to identify nematic electronic phases via diverging nematic sus-ceptibility to in-plane anisotropic strain in various iron-based superconductors [4,6,7]. Strain-induced phase transitions can be identified via resistivity scaling nematic critical points [8,9] and superconductor-insulator quantum phase transitions [10–12].

FeSe is a unique iron-based superconductor, which, despite its simple structure, hosts a nematic electronic phase in the ab-sence of a long-range magnetic order. This unusual electronic phase is driven by orbitally dependent effects and correla-tions that are responsible for unusual momentum-dependent band shifts [13–16]. The superconductivity emerging from this nematic phase has a twofold symmetric superconducting gap, orbitally selective pairing [16,17], and a spin-orbital-intertwined nematic state [18]. The nematic electronic phase

of FeSe is highly sensitive to external parameters, being strongly suppressed by the isoelectronic substitution with sul-fur [16,19] and external hydrostatic pressure, but, for higher applied pressure of ∼9 GPa, a robust superconducting phase with $T_c \sim 40$ K is stabilized, which competes with a spin-density wave [20].

A monolayer of FeSe, on a suitable substrate, can sustain superconductivity in excess of 65 K, driven by a strong inter-facial electron-phonon coupling, the charge transfer through the interface, and strain effects [21,22]. This remarkable su-perconducting state is drastically reduced as the number of layers increases and it is highly dependent on the annealing processes being reduced to close to 20 K for 50 unit cells [21,23]. Superconductivity is enhanced by anisotropic com-pression in thin films of FeSe on CaF$_2$, but is suppressed and resistivity increases for films thinner than 100 nm [24], similar to exfoliated flakes of FeSe in the absence of a substrate [25]. Thus, uniaxial strain studies can help to isolate and decouple the different essential components to enhance super-conductivity and provide important insight in understanding its interplay with the electronic nematic phase of FeSe.

In this paper, we explore how the electronic behavior of bulk single crystals FeSe is affected by uniaxial strain, using magnetotransport measurements outside and inside the ne-matic phase. We find that uniaxial strain induces significant changes in resistivity and its gradient is highly temperature dependent, being closely correlated with the Hall coefficient inside the nematic phase. The resistivity curves cross in a sin-gle point in the vicinity of the normal to the superconducting transition and we determine a strain-dependent scaling and its

*Corresponding author: michele.ghini@studio.unibo.it
†Corresponding author: amalia.coldea@physics.ox.ac.uk
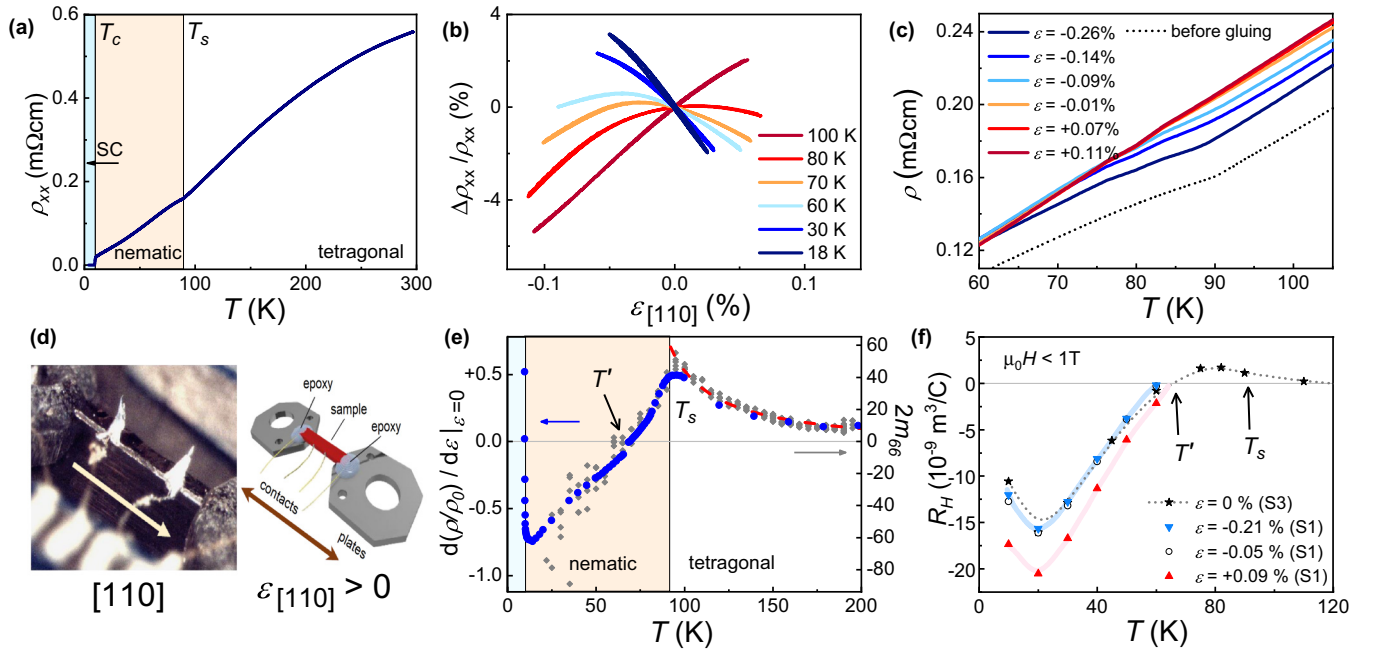
FIG. 1. (a) Transport measurement of the single crystal of FeSe with the current along the [110] tetragonal direction. (b) Relative changes in resistivity versus applied uniaxial strain at fixed temperatures around the structural transition T_s. (c) Resistivity measurements as a function of temperature around T_s at different fixed amounts of uniaxial strain. The dotted line is measured before gluing the sample to the strain cell. (d) Single crystal of FeSe glued with epoxy and suspended between the two titanium plates of the strain cell. (e) Slope of the linear fit of normalized resistivity against uniaxial strain $d(\rho/\rho_{\varepsilon=0})/d\varepsilon$ for $\varepsilon \to 0$, indicated by the solid blue symbols. The grey diamonds are the values of m_{66} normalized at 200 K and the dashed line is a fit to the Curie-Weiss law, after Ref. [6]. (f) Hall coefficient R_H, estimated as the low-field slope of the ρ_{xy} versus B below 1 T, under different constant uniaxial strain inside the nematic phase. Unstrained bulk measurements are indicated by the star symbols, after Ref. [26].

critical exponent. Our results under strain in single crystals of FeSe are consistent with those found for epitaxially grown FeSe films on different substrates. These results indicate that the superconducting state is enhanced under compressive strain and suppressed under tensile strain.

II. EXPERIMENTAL DETAILS

FeSe single crystals were grown by the chemical vapor transport method [27,28]. Electrical connections were made using indium soldering in a five-point-contact configuration for magnetotransport measurements. The current flows parallel to the direction of the applied stress, which is the [110] direction (Fe–Fe bonds) in the tetragonal symmetry and corresponds to the B_{2g} symmetry channel [29]. Strain experiments were performed using a CS100 cell from Razorbill [30]. The bar-shaped single crystal is suspended freely between two mounting plates and glued using a two-part epoxy, different from studies in which the sample is glued first to a thin titanium plate, which is itself strained and allows large strain to be applied [31]. As the material is very soft, the glue itself can also apply a small tensile strain to the sample ($\varepsilon_{glue} \sim 0.02\%$) [Fig. 1(d)], as found in previous NMR studies [32]. The capacitance between the two plates provides a direct estimate of the applied displacement (μm). The amount of nominal stress applied, $\varepsilon = \Delta L/L_0$ was of the order of 0.05–0.25% and the actual lattice distortion was calculated by finite element simulations, as shown in the Appendix.

III. RESULTS AND DISCUSSION

A. Resistivity under strain inside the nematic phase

Figure 1 shows the effect of the applied strain along the [110] tetragonal direction on the transport behavior of a single crystal of FeSe. In the absence of strain, FeSe enters the nematic phase below $T_s \sim 87$ K and it becomes superconducting at $T_c \sim 9$ K, having a large resistivity ratio between the room temperature resistivity and that at the superconducting onset (RRR ~ 27) [Fig. 1(a)], consistent with previous studies [6,33]. We performed detailed transport measurements as a function of uniaxial strain at fixed temperatures, as the strain cell is capable of applying large and tunable uniaxial stress at low temperatures. Figure 1(b) shows the relative variation in resistivity, $\Delta\rho_{xx}/\rho_{xx}(0) = [\rho_{xx}(\varepsilon) - \rho_{xx}(0)]/\rho_{xx}(0)$, at fixed temperatures inside and outside the nematic phase and in the vicinity of T_c. At high temperatures in the tetragonal phase, tensile strain (positive strain) increases the resistivity of the system while compressive strain (negative strain) decreases it. On the other hand, inside the nematic state, the response to strain changes significantly and becomes strongly nonlinear and the slope changes sign compared with the tetragonal phase.

Figure 1(e) shows the temperature dependence of the slope of the normalized resistance as a function of uniaxial strain in the limit of small strain ($S = d(\rho/\rho_{\varepsilon=0})/d\varepsilon$, $\varepsilon \to 0$), extracted from the data shown in Fig. 1(b). In this low-strain regime, the temperature dependence of the slope follows closely the divergent behavior of the nematic susceptibility,

$2m_{66}$, (measured using piezostacks) as approaching T_s. $2m_{66}$ provides a direct measure of the electronic nematic order parameter and its temperature dependence has a Curie-Weiss behavior, as reported previously in Ref. [6] [see diamond symbols in Fig. 1(e)] and Refs. [9,14]. Inside the nematic phase, the effect of applied strain is unusual and the slope S changes signs as a function of temperature. We identify a characteristic temperature, $T' \sim 70$ K, as the temperature at which the strain has the weakest effect on resistivity and the slope changes signs, as compared with the high temperature regime. This behavior is consistent with the sign change of m_{66} below 65 K [6,14] as well as the change in resistivity anisotropy induced by the strain of a PEEK substrate [34]. Remarkably, the change in anisotropy at T' coincides also with the temperature at which a large anisotropy develops in the local spin susceptibility, as detected from the line splitting of the Knight shift [18]. Thus, the changes in the anisotropy of the local magnetism are likely to affect the scattering and the coherent coupling between local spins and itinerant electrons.

To further address this, we look at magnetotransport measurements inside the nematic phase (raw data shown in Fig. 6 in the Appendix). To describe the nonlinear effects in magnetic field of ρ_{xx} and ρ_{xy}, a three-band model was employed to account for a small electronlike pocket, besides almost compensated hole and electron pockets [26]. In the presence of the applied strain, the overall magnetotransport behavior does not change significantly and still requires a multiband model to explain these features. These findings are in contrast to spectroscopic surface-sensitive studies under strain that involve the presence of a single (uncompensated) electron peanut-shaped pocket [35,36]. The mobility spectra for bulk FeSe suggest that under tensile strain the mobility of the dominant carriers increase, as shown in Figs. 6(c) and 6(d) in the Appendix, in agreement with mobilities of thin films of FeSe under strain [37]. Furthermore, the Hall coefficient of bulk FeSe, $R_H = \rho_{xy}/B$ ($B < 1$ T) shown in Fig. 1(f), becomes negative below 65 K under different uniaxial strains, similar to the unstrained case [26], suggesting significant changes in scattering below T'. However, in thin films that have a higher degree of disorder, the Hall coefficient is always positive as disorder hinders and averages out the effects responsible for the negative Hall coefficient [26,37,38]. An extremum of the Hall coefficient has been assigned to a maximum in the scattering anisotropy by spin fluctuations [39] or driven by the currents renormalized by vertex corrections dominated by the majority carriers [40]. Coupling with the lattice of these fluctuations may have additional consequences such as the suppression of superconductivity and of the nematic critical fluctuations [41–43].

To further understand the changes of the electronic structure under strain, we have calculated the Fermi surface of FeSe. Figure 8 shows the evolution of the Fermi surface with strain and for the renormalized and shifted band structure, which was brought in agreement with high temperature angle-resolved photoemission spectroscopy (ARPES) data [6]. Interestingly, the density functional theory (DFT) calculations [44] suggest that the in-plane anisotropy is larger for the electron bands whereas out-of-plane anisotropy changes for all pockets with increasing strain (Fig. 8 in the Appendix). The sizes and the number of charge carriers for all three pockets
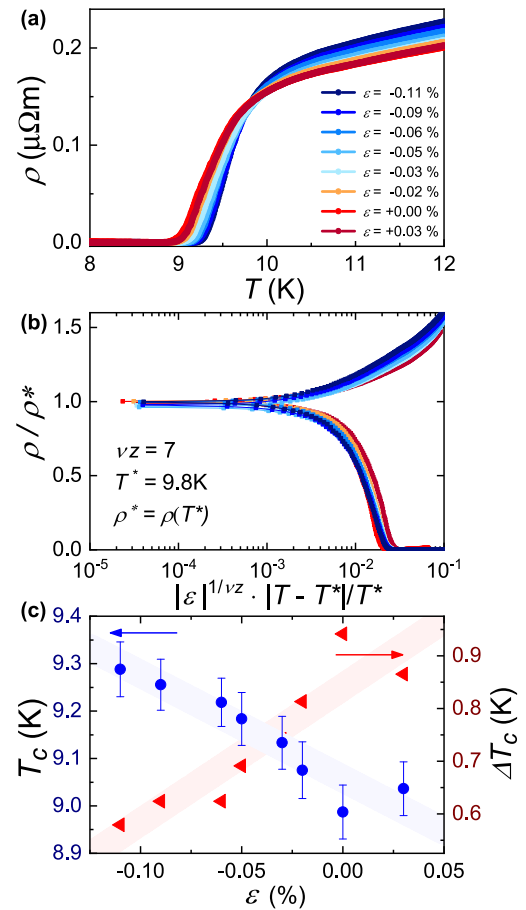
FIG. 2. (a) Temperature dependence of the resistivity near the superconducting to normal transition under uniaxial strain. The superconducting state is clearly enhanced under compressive uniaxial strain. Opposite trends are found for tensile strain, which can be detected from the constant temperature strain loops in Fig. 7(d) in the Appendix. As the sample is glued to the strain cell, it will be exposed to an additional small tensile strain, $\varepsilon_{glue} \sim 0.02\%$. (b) Scaling analysis of superconducting to normal resistivity near the crossing point, $T^* = 9.8$ K, where ρ^* is the resistivity at $\rho^* = \rho(T^*)$. The ratio between ρ/ρ^* versus $|\varepsilon|^{1/\nu z} \cdot |T - T^*|/T^*$ describes the universality of the transition with a critical exponent of $\nu z \approx 7$. (c) Variation of T_c, defined as the temperature with zero resistance, and of the width of the transition, ΔT_c, under applied strain. Solid lines are guides to the eye.

shrink with increasing strain, suggesting a potential increase in the Hall coefficient dominated by the most mobile carriers, as illustrated in Fig. 1(f) and Ref. [45]. ARPES studies in thin films of FeSe indicate that the tensile strain promotes significant shifts of the electron bands that can lead to the formation of highly mobile Dirac carriers [45]. Shifts of 2–3 meV under tensile strain can reduce the size of both electron and hole pockets [46]; the inner electron band could eventually disappear with increasing the strength of the orbital order [19].

Next, we focus on the effect of strain on the nematic transition at T_s shown in Fig. 1(c). In the absence of strain, there is a well-defined anomaly in resistivity at T_s, as shown in Fig. 5(e) in the Appendix. As the nematic order parameter and associated lattice distortion have a B_{2g} symmetry that

breaks the fourfold rotational symmetry, the applied uniaxial strain in FeSe along the [110] tetragonal direction induces a finite order parameter at all temperatures. Therefore, it turns the phase transition into a crossover, smearing all the related features at T_s and the resistivity increases under tensile strain, as the scattering from nematic domain boundaries becomes significant. Interestingly, this effect is in the opposite direction to what happens in the vicinity of the superconducting transition where resistivity in the normal state is reduced due to tensile strain, as shown in Fig. 2(a). In our bulk FeSe, the sharp transition at T_s is suppressed from 87 K toward 83 K and replaced by a broad crossover with uniaxial stress (in addition to the effect of the glue that applies $\varepsilon_{glue} \sim 0.02\%$ [Figs. 5(e) and 5(f) in the Appendix] . After applying compressive strain, the resistivity is reduced and the curves seem to recover the signature of the unstrained sample, as shown in Fig. 1(c). This behavior is similar to that found for underdoped Co-doped $BaFe_2As_2$, where the feature corresponding to the nematic phase transition is quickly suppressed (under small strain of 3×10^{-3}) and replaced by a broad crossover [5]. In contrast, the ε_{B1g} strain is a continuous tuning parameter and has a quadratic variation as a function of strain for underdoped Co-doped $BaFe_2As_2$ [5].

B. Resistivity scaling under strain at low temperatures

Figure 2(a) shows the resistivity $\rho(T, \varepsilon)$ of bulk FeSe as a function of the temperature, under various amounts of uniaxial applied strain in the vicinity of the superconducting transition. In the normal state the resistivity decreases under tensile strain, as the mobility of the dominant carriers increases [Fig. 6(d) in the Appendix]. We find that all resistivity curves, independent from the amount of uniaxial strain applied, cross through a single point in the vicinity of the superconducting transition around $T^* \sim 9.8$ K. Using finite-size scaling analysis, all data can collapse onto a single curve by rescaling the resistivity with the value at the crossing point $\rho^* = \rho(T^*)$ and plotting it against the functional relation $|\varepsilon|^{1/\nu z}|T - T^*|/T^*$, as shown in Fig. 2(b). Scaling allows the determination of the critical exponents and the universality class of the transition [47]. The best results for bulk FeSe under strain are for a value of $\nu z \approx 7$, as shown in Fig. 7 in the Appendix, larger than $\nu z \approx 7/3$ found for dirty thin films of FeSe, which describes the universality class of quantum percolation transitions [10].

Scaling relations to describe superconductor-insulator quantum phase transitions [10–12] and superconductor-metal transitions report values of νz ranging from 0.3 to 8 [48]. Large values of νz can occur when the dynamical critical exponent shows a divergence by approaching the zero-temperature quantum critical point, as in the case of a Griffiths singularity [48]. A Griffiths phase can be found in the vicinity of a critical point in the presence of disorder for a two-dimensional superconductor-metal quantum phase transition; in this case, rare superconducting regions could form in the normal matrix both as a function of temperature and strain. Signatures of Griffiths phases have also been detected in the vicinity of a nematic critical point in $FeSe_{0.89}S_{0.11}$ tuned by magnetic field and applied hydrostatic pressure [49]. Our findings suggest that strain leads to a superconducting-to-insulating phase transition in bulk FeSe with the possible
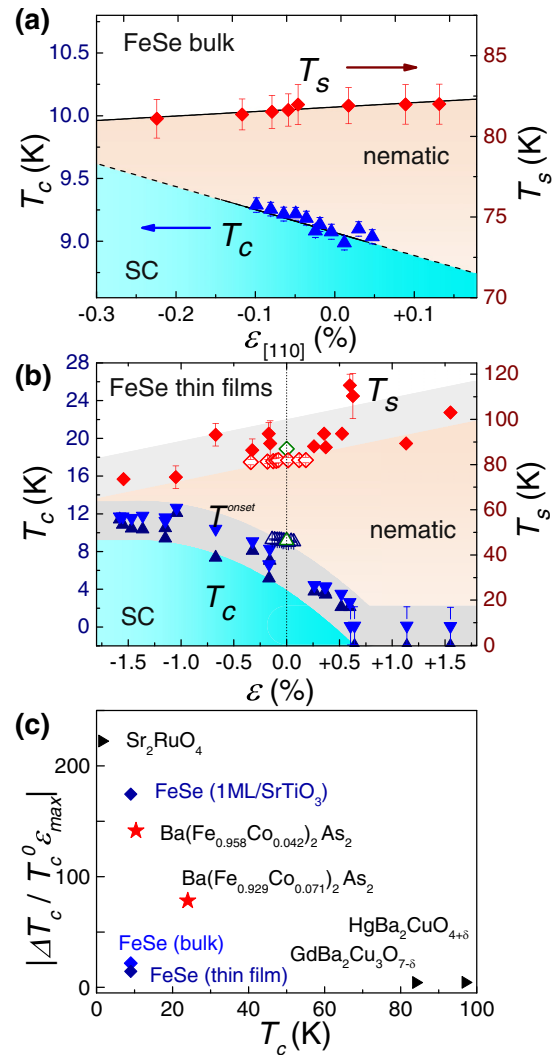
FIG. 3. Superconducting phase diagrams versus strain of (a) bulk FeSe based on this study and (b) thin films of FeSe epitaxially growth on different substrates, adapted after Ref. [37]. Panel (b) contains the single crystal data (open symbols) from (a), which are adjusted to include the additional small tensile strain caused by the glue $\varepsilon_{glue} \sim 0.02\%$. Compressive strain ($\varepsilon < 0$) enhances superconductivity and seems to suppress the nematic state. Black data points in (b) refer to T_s and T_c of bulk FeSe. (c) The sensitivity of T_c to strain, $\Delta T_c/(\varepsilon_{max} \cdot T_c^{\varepsilon=0})$, for a variety of unconventional superconductors, adapted after Ref. [2] and compared with bulk, thin films of FeSe and monolayers of FeSe on $SrTiO_3$.

formation of inhomogeneous superconducting regions inside the normal matrix. This important role played by strain and the consequent coupling with the lattice is likely to have an effect on the critical fluctuations of iron-chalcogenides [42].

C. Phase diagram of FeSe under uniaxial strain

The resistivity studies of bulk FeSe under strain have revealed that the compressive strain enhances superconductivity and narrows the width of the superconducting transition, as shown in Figs. 2(a) and 2(c). Under tensile strain, FeSe displays a superconductor-to-metal quantum phase transition

[see also Fig. 5(d) in the Appendix], similar to underdoped iron-pnictides [2]. Figure 3 shows the phase diagrams for bulk FeSe under strain and thin films of FeSe epitaxially strained by different substrates. For thin films, the strain is mainly induced by the mismatch in the lattice parameters between the film and the substrate [37,50]. Interestingly, the compressive uniaxial strain enhances superconductivity but it seems to suppress the nematic phase for both bulk and epitaxial films, suggesting that the two phases are competing with each other, similar to what is found under small applied hydrostatic and chemical pressure [16,19,51] However, these opposite trends of the superconductivity versus nematicity under strain are in contrast to the effect of growth conditions and disorder [33]. In thin flakes of FeSe, T_s and T_s decrease at the same time [25], suggesting that disorder as well as scattering of twin boundary formations inside the nematic phase may have an important role on the transport behavior.

The response of the superconductivity of FeSe to strain can be compared with that of Co-doped $BaFe_2As_2$ single crystals [2]. For underdoped and near-optimally doped compositions, the superconducting critical temperature has a quadratic dependence on applied strain being rapidly suppressed by both compressive and tensile stress ε_{B2g}. In the overdoped regime, the response of T_c to strain is smaller in magnitude and no longer symmetric for tensile and compressive stress, resembling the behavior found for FeSe, which has a nematic phase but no long-range order, similar to overdoped pnictides [Fig. 3(c)]. The sensitivity to strain of T_c in bulk FeSe agrees with uniaxial high-resolution thermal-expansion measurements which suggests that superconductivity couples strongly to the in-plane area [28], being anisotropic for the two in-plane directions ($dT_c/dp_a = 2.2(5)$ K/GPa and $dT_c/dp_b = 3.1(1.1)$ K/GPa [28]) whereas under uniaxial strain dT_c/da is ∼54 K/Å [Fig. 3(c)]. Thus, to stabilize a 90 K superconductor, the applied uniaxial strain needs to be extremely large, much higher than the strain generated by a $SrTiO_3$ substrate. This suggests that strain on its own is insufficient to enhance superconductivity and electron doping plays an essential role.

IV. CONCLUSIONS

To summarize, we have investigated the electronic response to external uniaxial strain of bulk single crystals of FeSe. We have identified a direct correlation between the transport response to strain, which is is strongly temperature dependent, and the temperature changes in the Hall coefficient. The normal resistivity increases under tensile strain in the vicinity of the nematic transition but it decreases in the proximity of the superconducting transition. This suggests that there is a strong coupling between different scattering processes which are strongly temperature dependent involving the formation of nematic domains, multiband effects, and the coupling with the lattice. Band-structure calculations suggest that under strain the electron bands would develop the largest in-plane anisotropy. Superconductivity of FeSe is enhanced under compressive uniaxial strain, similar to overdoped 122 iron-based superconductors, whereas the the nematic electronic state responds to strain in an opposite way. Furthermore, close to the critical temperature, we identify a universal crossing point for all resistivity curves measured un-
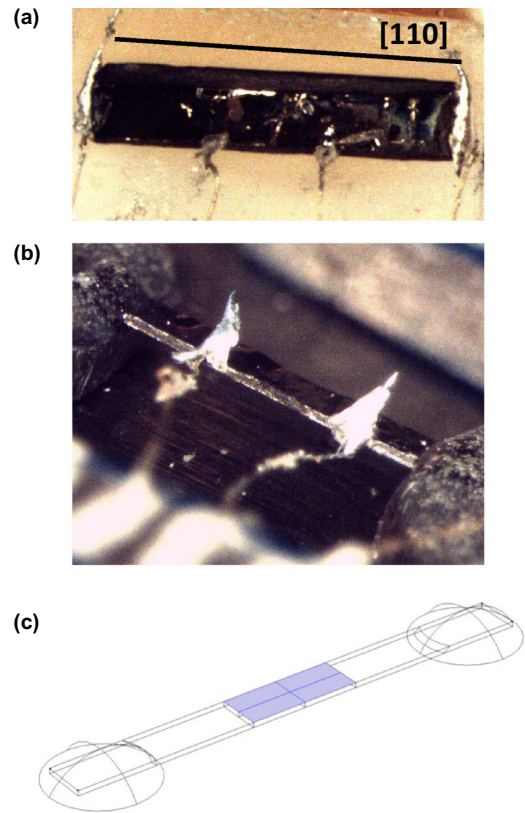
FIG. 4. (a) Freestanding single crystals of FeSe cut along the [110] tetragonal direction measured before being mounted on the strain cell in (b). (c) The sample model used to estimate the strain transmission in the sample inside the cell strain secured at both ends by epoxy.

der constant strain. The scaling behavior of resistivity versus temperature in the vicinity of the superconducting transition indicates the existence of a strain-induced phase transition that would be consistent with the development of rare superconducting regions inside of a normal metal matrix as a function of temperature and strain. This study establishes that uniaxial strain, on its own, is not sufficient to stabilize a high-T_c FeSe-based superconductor.

In accordance with the EPSRC policy framework on research data, access to the data will be made available from https://ora.ox.ac.uk/objects/uuid:30297572-0b91-4411-8213-f8c68621ad3f.

Note in proofs: After completing this work, we become aware of another study of FeSe under strain [55], in which the single crystals are glued to titanium sheets and these platforms are strained to higher values that would be possible for a stand-alone crystal (as in our study). The reported findings are in broad agreement with the results presented in our work.
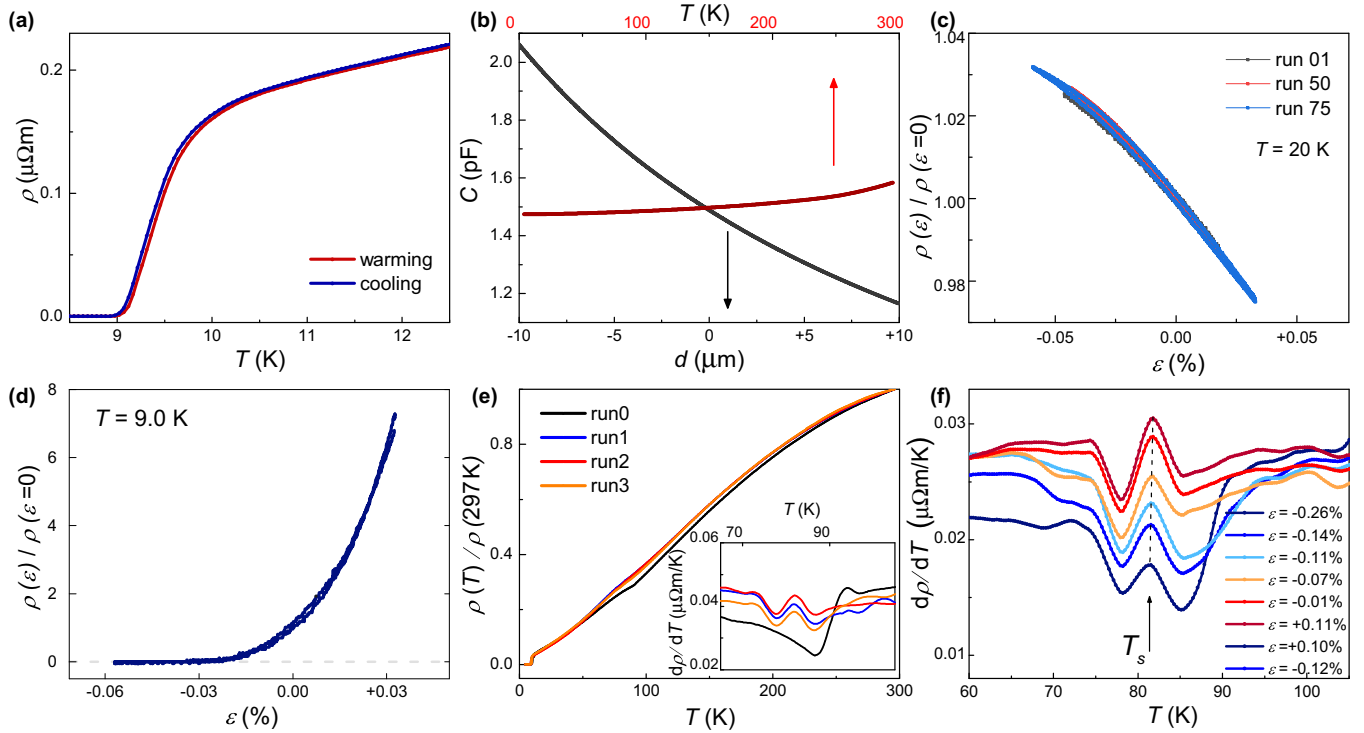
FIG. 5. (a) Transport measurements performed while cooling and warming, showing the small temperature variations are due to the thermal load of the strain cell. (b) Capacitance as a function of the displacement d (μm) of the two plates, calculated at room temperature (in black). Temperature dependence of the capacitance without any external strain applied (in red). (c) Resistance versus strain at 20 K, indicating the reproducibility and consistency between different measurements acquired at the same temperature. (d) Direct evidence that compressive strain enhances the superconducting state, showing the superconducting to normal transition induced by uniaxial compressive strain at fixed temperature $T = 9.0$ K. (e) Transport measurements without applied strain at different stages of the experiment. All the values are normalized at room temperature $\rho(T)/\rho(\mathrm{RT})$. Inset shows the derivative of the resistivity against temperature of the same runs, indicating the smearing of the transition after gluing the sample to the strain cell as compared with the freestanding sample (run 0). (f) Derivative of resistivity against temperature around the nematic transition at different applied strains. The structure of the transition developed an additional feature after the gluing of the sample to the strain cell. Here, T_s is defined as the position of the Gaussian fit of the middle peak.

APPENDIX

1. Strain calibration and simulations

Hysteresis strain loops were performed at constant temperature to investigate the sample response to uniaxial tensile and compressive stress. The hysteresis loops were performed at least twice for each set temperature. Multiples measurements were conducted on the sample over several weeks to verify reproducibility between different measurements [Fig. 5(c)].

FeSe crystals, with typical dimensions of $\approx 1100 \times 500 \times 60~\mu$m^3, were cut into a rectangular shape along the [110] tetragonal direction, which corresponds to applying strain

along the B_{2g} symmetry channel [29], and mounted on the CS100 uniaxial strain cell. The amount of nominal stress applied, $\varepsilon_{\mathrm{external}} = \Delta L / L_0$, is defined as the displacement $\Delta L = L(T) - L_0(T)$ divided by the unstrained length L_0 of the sample. An ultraprecise capacitance sensor (Andeen-Hagerling AH270 Capacitance bridge) was used to measure the position of the two titanium plates, in order to evaluate the amount of strain applied with the uniaxial strain cell. Capacitance as a function of the distance between two plates follows the equation: $C(d) = \varepsilon_{\mathrm{external}} A / [d + d_{\mathrm{cell}}]$, with $d_{\mathrm{cell}} = 36.00~\mu$m, $A = 6.04$ mm^2, $\varepsilon_{\mathrm{external}} = \varepsilon_0 \times k = 8.8586$ pF/m, and where d is the displacement applied from the cell.

To asses the strain transmission through the sample and quantify the internal strain compared to the applied stress, we have performed finite element analysis simulations in COMSOL using the linear elastic material model from the structural mechanics module, testing our approach against previous reports [53]. The geometry was constructed and parameterized to match the geometry of the sample as shown in Fig. 4. $\varepsilon_{\mathrm{external}}$ was averaged over the the volume between the voltage contacts to get a value for the fraction of strain applied that is transmitted to the sample and averaged over the top and
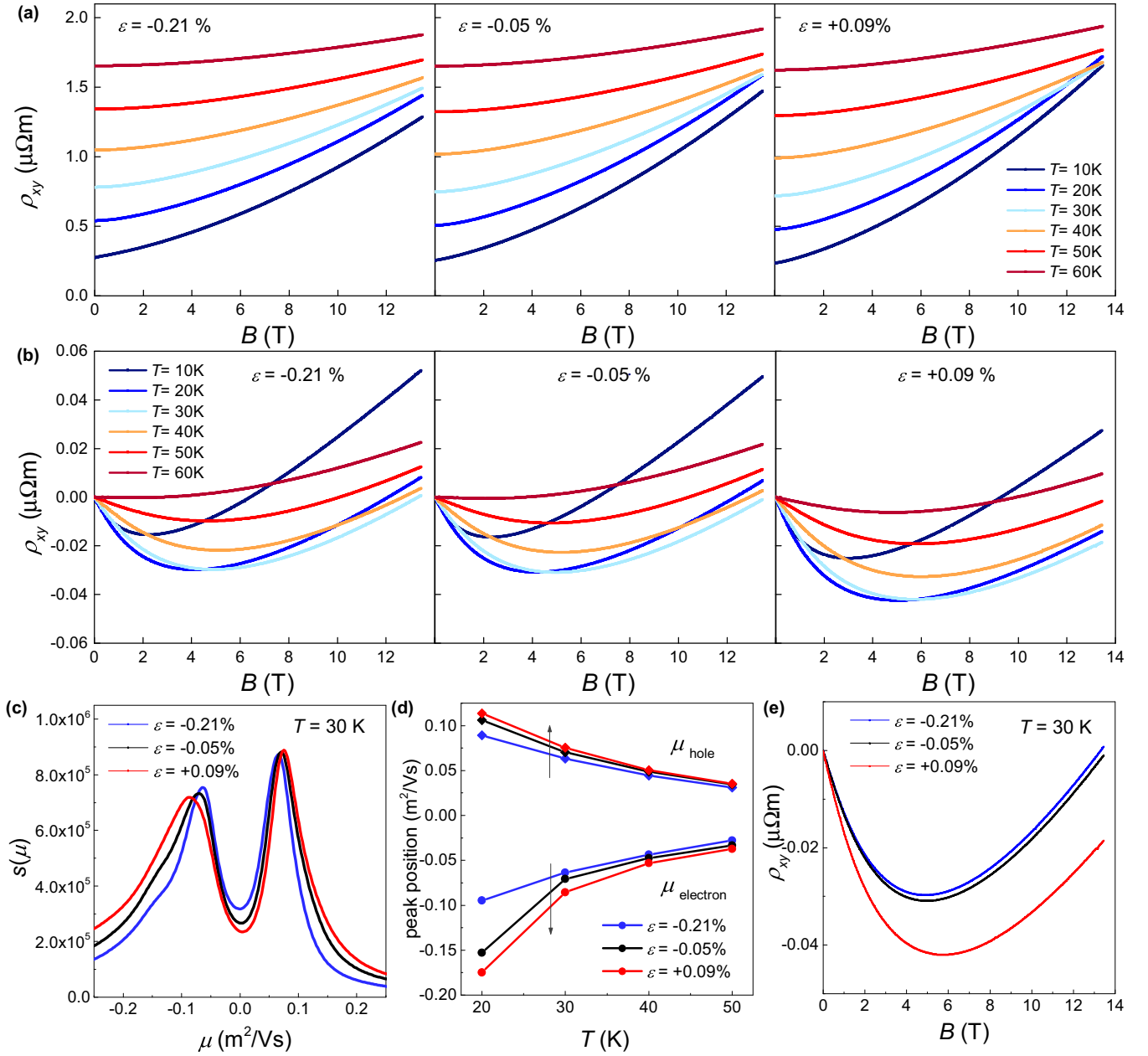
FIG. 6. (a) The longitudinal resistivity, ρ_{xx}, and (b) Hall component, ρ_{xy}, measured under different constant uniaxial strain applied along [110] axis for FeSe at constant temperatures inside the nematic phase. (c) Mobility spectrum at 30 K extracted from (a) and (b) for different values of uniaxial strain. (d) The position of the main peaks from the mobility spectrum for the main electron and hole in the range 20K-50K. For both carriers, tensile strain increases the mobility (in terms of absolute values) while compressive strain tends to decrease it. (e) Direct comparison between the Hall component ρ_{xy} for different strain at 30 K.

bottom surfaces between the contacts to get a value for the strain inhomogeneity across the sample. For the parameters used, $\varepsilon_{[110]} = 0.7146 \; \varepsilon_{\text{external}}$. The strain generated by the epoxy was also simulated and contributes a tensile strain of about $\varepsilon_{\text{glue}} \sim 0.02\%$ to the sample.

To extract the value of nominal strain from the measured capacitance, we account for its temperature dependence (the thermal contractions of titanium were negligible). Figure 5(b) shows the behavior of the capacitance against the displacement of the two plates $C(d)$ at room temperature and the dependence of the capacitance sensor versus temperature. Various measurements were carried out over the tempera-

ture range $\Delta T = 3 - 300\,\text{K}$ without any applied strain (zero voltage applied to the piezostacks) to establish the trend of $C(T, d_0)$. To account for this effect, the corrected capacitance is obtained by subtracting from the measured capacitance at a given temperature the variation in capacitance between that temperature and room temperature.

As bulk FeSe is a soft layered material, large amounts of strain tend to break the sample. Bending, cracking, and exfoliation were observed in various samples with this suspended configuration for higher values of stress. Figure 5(e) shows the resistivity of the sample without applied strain in different stages of the experiment: before and after gluing the
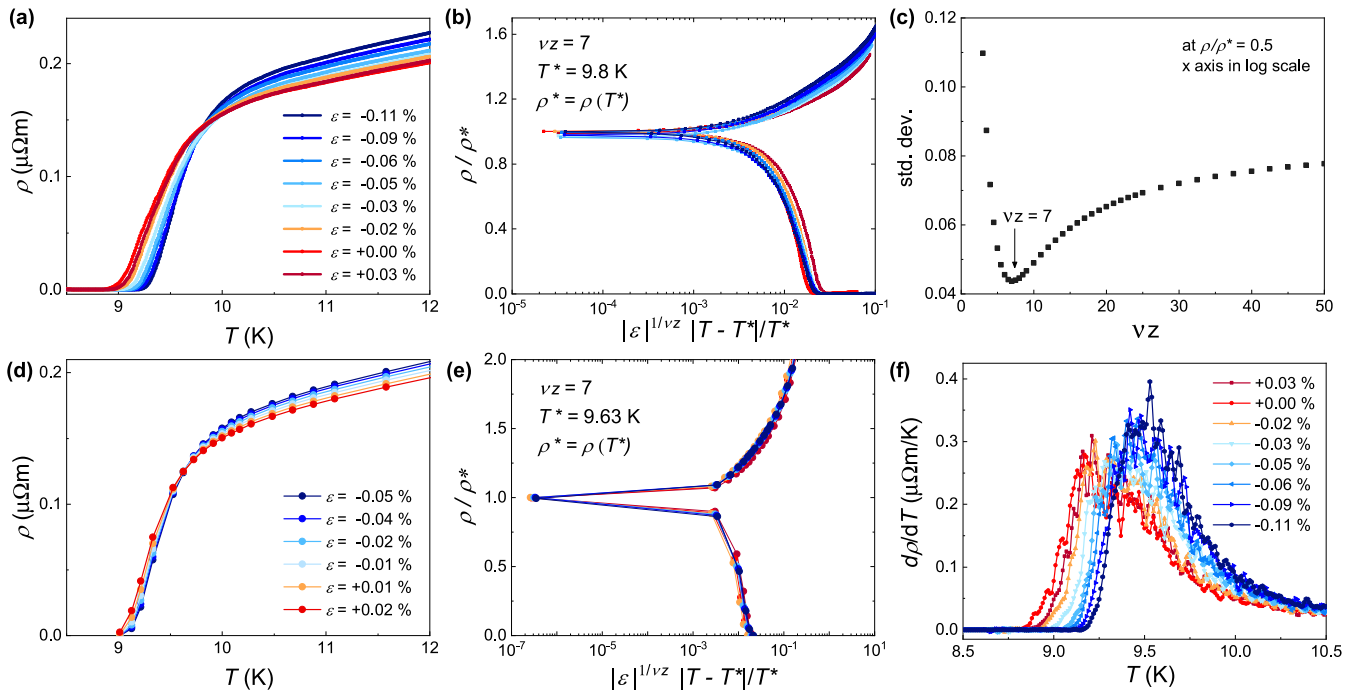
FIG. 7. (a) Temperature dependence of the resistivity near the superconductive transition, measurements performed by varying the temperature while keeping constant the applied strain. Negative uniaxial strain (compressive) increases the resistivity while positive uniaxial strain (tensile) has an opposite effect. The superconductive state is slightly enhanced under compressive strain and suppressed under tensile strain. (b) Scaling analysis of (a) near the crossing point at $T^* = 9.8$ K, where ρ^* is the resistivity at the critical point $\rho^* = \rho(T = T^*)$. The ratio between ρ/ρ^* versus the functional relation $|\varepsilon|^{1/\nu z}|T - T^*|/T^*$ is able to describe the universality of the transition with a critical exponent of $\nu z \approx 7$. (c) Width of the dispersion of the scaling analysis at $\rho/\rho^* = 0.5$ as a function of the critical exponent of νz, for measurements conducted at fixed applied strain [from (b)]. (d) Resistivity near the superconductive transition, with different amounts of applied uniaxial strain. The measurements conducted at constant temperature to confirm findings from previous measurements performed at constant strain. (e) Scaling analysis of (d) near the crossing point at $T^* = 9.63$ K, from the data collected at constant temperature with an exponent of $\nu z \approx 7$, similar to that illustrated in (b). (f) The first derivative of the data in (a), showing the evolution of width of the superconducting transition with uniaxial strain.

sample to the cell (run 0 and run 1), after all the measurements without magnetic field (run 2), and after the last measurement (run 3). The behavior of the system is consistent between all the different runs (measured over several weeks) but the first one, which corresponds to the freestanding case which was not glued to the cell. Figure 5(f) illustrates the derivative of resistivity versus temperature in the proximity of the nematic transition, showing the impact of glue on transport properties. It is possible to observe the evolution of T_s under the effect of the applied strain by assessing the shifts of the high-temperature minimum as well as the position of the middle peak.

For a limited temperature range in which the capacitance of the cell remains constant, resistivity measurements at constant strain were performed as a function of temperature. Precautions were taken to avoid unwanted effects of thermal drift and fluctuation. All transport measurements as a function of temperature reported in this paper were collected during warming ramps and with slow warming rates to limit effects of the thermal load at low temperatures. Figure 5(a) shows the thermal drift of a cooling ramp compared to the warming measurement. Figure 5(d) shows the transition between the superconducting to normal state induced by the uniaxial compressive strain at a fixed temperature ($T = 9.0$ K).

2. Magnetotransport studies

Magnetotransport measurements were conducted as a function of the magnetic field up to 13.5 T inside the nematic phase (between $T = 10$ K and $T = 60$ K), under three different amounts of uniaxial strain between $\varepsilon = -0.21\%$ to $+0.09\%$. Magnetotransport measurements were conducted measuring both the longitudinal resistivity, ρ_{xx}, (with the current along the [110] direction), and the Hall component, ρ_{xy}, as a function of the applied magnetic field applied along the [0 0 1] direction. These values have been symmetrized and antisymmetrized, with respect to the applied magnetic field (as reported in Figs. 6(a) and 6(b). Figure 6(c) reports the mobility spectrum generated from the magnetotransport data for different amounts of strain at $T = 30$ K. The mobilities of the dominant charge carriers are consistently enhanced under tensile strain and suppressed under compressive strain, inside the nematic phase [Fig. 6(d)]. The low field Hall coefficient, R_{H} (in $B < 1$T), is surprisingly insensitive to compressive strain but changes under tensile strain, as shown in Fig. 6(e).

3. Scaling analysis

Figure 7 reports scaling of the reduced resistivity ρ/ρ^* around the strain-independent crossing point T^* as a func-
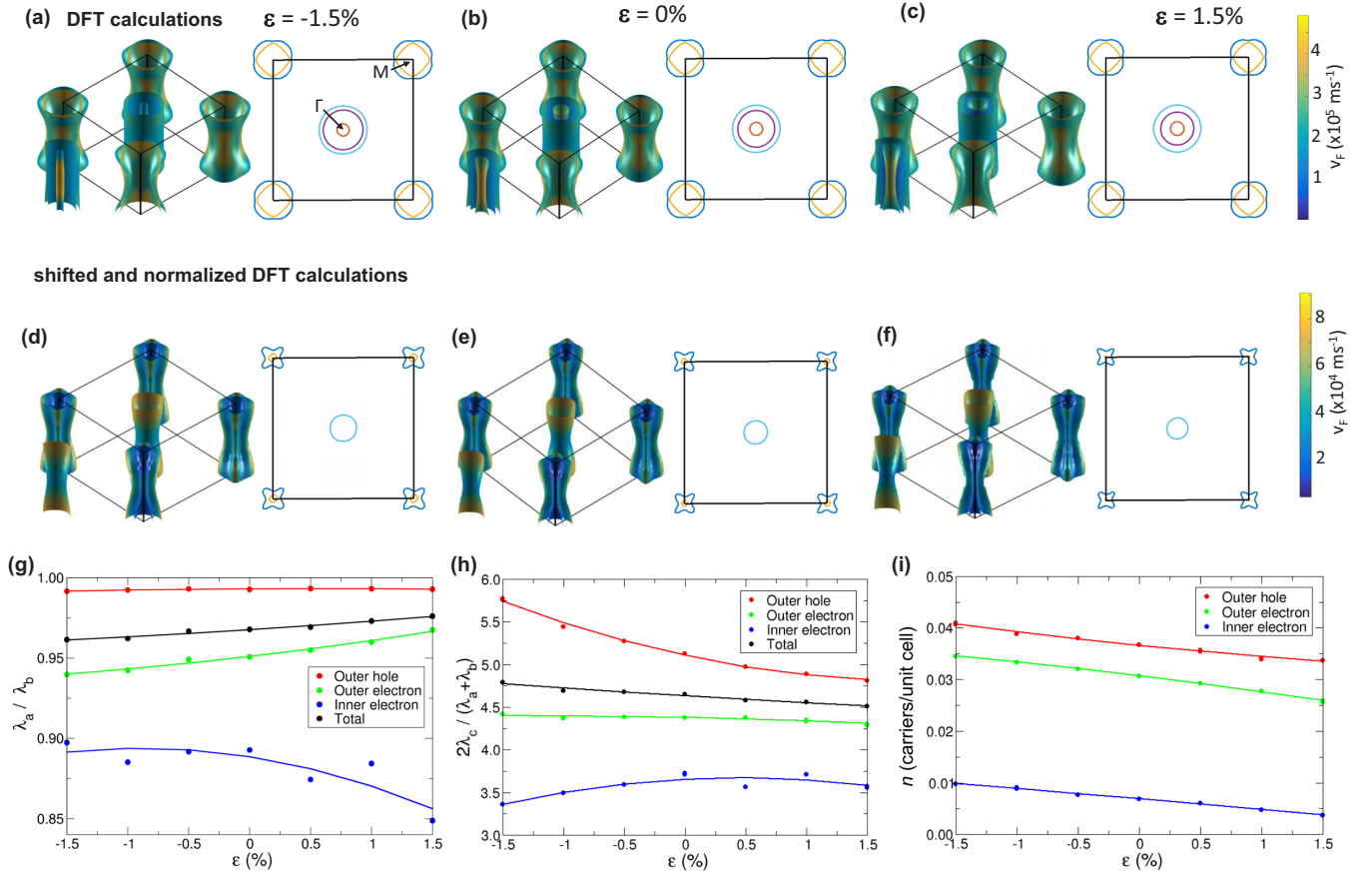
FIG. 8. Calculated Fermi surface plots and slices through the center of the Brillouin zone (Γ-M plane) for FeSe for different applied strain ε along [110] of $\varepsilon = -1.5\%$ in (a), (d), $\varepsilon = 0\%$ in (b), (e), and $\varepsilon = 1.5\%$ in (c), (f). 3D Fermi surface plots are colored by the magnitude of the Fermi velocity. Color bars for each row are displayed on the far right. Panels (a)–(c) show the Fermi surface with increasing strain as calculated in WIEN2K using the GGA approximation (PBE functional) [44,54], including the spin-orbit coupling. We use the experimental orthorhombic parameters (*Cmma* symmetry and $a = 5.308$ Å, $b = 5.334$ Å, $c = 5.486$ Å and the volume cell of the unit cell is conserved under applied uniaxial strain. Panels (d)–(f) show the Fermi surface after band renormalization and shifting are applied to match the unstrained experimental ARPES data at high temperatures above T_s [6]. Band renormalization of 3 and 4 are applied to the outer hole band at Γ and both electron bands at M, respectively, and a band shift of 45 meV is applied to the electron bands and −45 meV is applied to the hole band to ensure charge compensation, as suggested by previous experimental ARPES data [6]. (g) In-plane and (h) out-of-plane anisotropy of the penetration depth. (i) The number of charge carriers per unit cell for each quasi-two-dimensional cylinder of each shifted Fermi surface pocket as a function of strain. The solid lines are guides to the eye.

tion of $|\varepsilon|^{1/\nu z}|T - T^*|/T^*$ [Fig. 7(b)]. This functional relation leads to a collapse of the experimental data with the same exponent $\nu z \approx 7$. Figure 7(c) reports the standard deviation of the dispersion at $\rho/\rho^* = 0.5$ versus different values of the critical exponent νz as a way to estimate the optimal exponent. Optimal results were obtained with a value close to the minimum $\nu z = 7$. Figure 7(d) shows transport measurements at the superconductive transition collected by varying the uniaxial strain at fixed temperatures, instead of varying the temperature with fixed strain. As before, we observe that compressive strain increases the resistivity above the transition and enhances the superconductive state (while tensile strain induces opposite effects) and the presence of the temperature T^* at the middle of the transition.

4. Band-structure calculations

Figures 8(a)–8(c) report Fermi surfaces and slices through the center of the Brillouin zone (Γ-M plane) for bulk FeSe for

different applied strain along [110] of $\varepsilon = \pm 1.5\%$. The same renormalizations and band shifts were chosen to agree with ARPES data in the unstrained tetragonal case [6] and these shift were applied at all calculations under strain [Figs. 8(d)–8(f)]. The outer hole band and the two electron bands were renormalized by a factor of 3 and 4, respectively, as suggested by ARPES data [6], and then shifted by −45 meV and 45 meV, respectively, to ensure charge compensation. Additionally, the inner and middle hole bands are shifted away from the Fermi level entirely, as compared with the unshifted case [Figs. 8(a)–8(c)]. We find that both the outer hole band and the electron bands shrink with increasing tensile strain in both the unshifted and shifted cases. This reflects clearly in the number of charge carriers that decreases with increasing tensile strain for all three Fermi surface pockets, as shown in Fig. 8(i).

The understand the effect of the strain on the in-plane and out-of-plane anisotropy of the Fermi surface pockets, we have also computed the penetration depth, λ, along the

three lattice vectors, and taking suitable ratios. Figure 8(g) shows the in-plane anisotropy (λ_a/λ_b) and Fig. 8(h) shows the out-of-plane anisotropy $2\lambda_c/(\lambda_a + \lambda_b)$), calculated from the renormalized and shifted Fermi surface pockets for several values of strain. The inner electron pocket is much smaller than the others, so numerical errors affect the results much more strongly, as seen. We find that the hole pocket is es-

sentially isotropic in-plane, while the electron pockets have some in-plane anisotropy. However, all three pockets exhibit out-of-plane anisotropy, with the hole band exhibiting the largest anisotropy. The anisotropy in the overall penetration depth, calculated by combining the contributions from each pocket, remains fairly constant with strain, both in plane and out of plane.

[1] A. Steppke, L. Zhao, M. E. Barber, T. Scaffidi, F. Jerzembeck, H. Rosner, A. S. Gibbs, Y. Maeno, S. H. Simon, A. P. Mackenzie, and C. W. Hicks, Strong peak in T_c of Sr_2RuO_4 under uniaxial pressure, Science **355**, eaaf9398 (2017).

[2] P. Malinowski, Q. Jiang, J. J. Sanchez, J. Mutch, Z. Liu, P. Went, J. Liu, P. J. Ryan, J.-W. Kim, and J.-H. Chu, Suppression of superconductivity by anisotropic strain near a nematic quantum critical point, Nat. Phys. **16**, 1189 (2020).

[3] A. E. Böhmer, A. Sapkota, A. Kreyssig, S. L. Bud'ko, G. Drachuck, S. M. Saunders, A. I. Goldman, and P. C. Canfield, Effect of Biaxial Strain on the Phase Transitions of $Ca(Fe_{1-x}Co_x)_2As_2$, Phys. Rev. Lett. **118**, 107002 (2017).

[4] J.-H. Chu, H.-H. Kuo, J. G. Analytis, and I. R. Fisher, Divergent nematic susceptibility in an iron arsenide superconductor, Science **337**, 710 (2012).

[5] M. S. Ikeda, T. Worasaran, J. C. Palmstrom, J. A. W. Straquadine, P. Walmsley, and I. R. Fisher, Symmetric and antisymmetric strain as continuous tuning parameters for electronic nematic order, Phys. Rev. B **98**, 245133 (2018).

[6] M. D. Watson, T. K. Kim, A. A. Haghighirad, N. R. Davies, A. McCollam, A. Narayanan, S. F. Blake, Y. L. Chen, S. Ghannadzadeh, A. J. Schofield, M. Hoesch, C. Meingast, T. Wolf, and A. I. Coldea, Emergence of the nematic electronic state in FeSe, Phys. Rev. B **91**, 155106 (2015).

[7] K. Ishida, M. Tsujii, S. Hosoi, Y. Mizukami, S. Ishida, A. Iyo, H. Eisaki, T. Wolf, K. Grube, H. v. Löhneysen, R. M. Fernandes, and T. Shibauchi, Novel electronic nematicity in heavily hole-doped iron pnictide superconductors, Proc. Natl. Acad. Sci. **117**, 6424 (2020).

[8] H.-H. Kuo, J.-H. Chu, J. C. Palmstrom, S. A. Kivelson, and I. R. Fisher, Ubiquitous signatures of nematic quantum criticality in optimally doped Fe-based superconductors, Science **352**, 958 (2016).

[9] S. Hosoi, K. Matsuura, K. Ishida, H. Wang, Y. Mizukami, T. Watashige, S. Kasahara, Y. Matsuda, and T. Shibauchi, Nematic quantum critical point without magnetism in $FeSe_{1-x}S_x$ superconductors, Proc. Natl. Acad. Sci. U.S.A. **113**, 8139 (2016).

[10] R. Schneider, A. G. Zaitsev, D. Fuchs, and H. v. Löhneysen, Superconductor-Insulator Quantum Phase Transition in Disordered FeSe Thin Films, Phys. Rev. Lett. **108**, 257003 (2012).

[11] J.-Y. Lin, Y. S. Hsieh, D. A. Chareev, A. N. Vasiliev, Y. Parsons, and H. D. Yang, Coexistence of isotropic and extended *s*-wave order parameters in FeSe as revealed by low-temperature specific heat, Phys. Rev. B **84**, 220507(R) (2011).

[12] X. Shi, P. V. Lin, T. Sasagawa, V. Dobrosavljević, and D. Popović, Two-stage magnetic-field-tuned superconductor-insulator transition in underdoped $La_{2-x}Sr_xCuO_4$, Nat. Phys. **10**, 437 (2014).

[13] S.-H. Baek, D. V. Efremov, J. M. Ok, J. S. Kim, J. van den Brink, and B. Büchner, Orbital-driven nematicity in FeSe, Nat. Mater. **14**, 210 (2015).

[14] M. A. Tanatar, A. E. Böhmer, E. I. Timmons, M. Schütt, G. Drachuck, V. Taufour, K. Kothapalli, A. Kreyssig, S. L. Bud'ko, P. C. Canfield, R. M. Fernandes, and R. Prozorov, Origin of the Resistivity Anisotropy in the Nematic Phase of FeSe, Phys. Rev. Lett. **117**, 127001 (2016).

[15] A. E. Böhmer, T. Arai, F. Hardy, T. Hattori, T. Iye, T. Wolf, H. v. Löhneysen, K. Ishida, and C. Meingast, Origin of the Tetragonal-to-Orthorhombic Phase Transition in FeSe: A Combined Thermodynamic and NMR Study of Nematicity, Phys. Rev. Lett. **114**, 027001 (2015).

[16] A. I. Coldea and M. D. Watson, The key ingredients of the electronic structure of FeSe, Annu. Rev. Condens. Matter Phys. **9**, 125 (2018).

[17] P. O. Sprau, A. Kostin, A. Kreisel, A. E. Böhmer, V. Taufour, P. C. Canfield, S. Mukherjee, P. J. Hirschfeld, B. M. Andersen, and J. C. Séamus Davis, Discovery of orbital-selective Cooper pairing in FeSe, Science **357**, 75 (2016).

[18] J. Li, B. Lei, D. Zhao, L. P. Nie, D. W. Song, L. X. Zheng, S. J. Li, B. L. Kang, X. G. Luo, T. Wu, and X. H. Chen, Spin-Orbital-Intertwined Nematic State in FeSe, Phys. Rev. X **10**, 011034 (2020).

[19] A. I. Coldea, Electronic nematic states tuned by isoelectronic substitution in bulk $FeSe_{1-x}S_x$, Front. Phys. (2021), doi:10.3389/fphy.2020.594500.

[20] S. Medvedev, T. M. McQueen, I. A. Troyan, T. Palasyuk, M. I. Eremets, R. J. Cava, S. Naghavi, F. Casper, V. Ksenofontov, G. Wortmann, and C. Felser, Electronic and magnetic phase diagram of β-$Fe_{1.01}Se$ with superconductivity at 36.7 K under pressure, Nat. Mater. **8**, 630 (2009).

[21] D. Huang and J. E. Hoffman, Monolayer FeSe on $SrTiO_3$, Annu. Rev. Condens. Matter Phys. **8**, 311 (2017).

[22] S. N. Rebec, T. Jia, C. Zhang, M. Hashimoto, D.-H. Lu, R. G. Moore, and Z.-X. Shen, Coexistence of Replica Bands and Superconductivity in FeSe Monolayer Films, Phys. Rev. Lett. **118**, 067002 (2017).

[23] Z. Wang, C. Liu, Y. Liu, and J. Wang, High-temperature superconductivity in one-unit-cell FeSe films, J. Phys.: Condens. Matter **29**, 153001 (2017).

[24] F. Nabeshima, Y. Imai, M. Hanawa, I. Tsukada, and A. Maeda, Enhancement of the superconducting transition temperature in FeSe epitaxial thin films by anisotropic compression, Appl. Phys. Lett. **103**, 172602 (2013)s.

[25] L. S. Farrar, M. Bristow, A. A. Haghighirad, A. McCollam, S. J. Bending, and A. I. Coldea, Suppression of superconductivity and enhanced critical field anisotropy in thin flakes of FeSe, npj Quantum Mater. **5**, 29 (2020).

[26] M. D. Watson, T. Yamashita, S. Kasahara, W. Knafo, M. Nardone, J. Béard, F. Hardy, A. McCollam, A. Narayanan, S. F. Blake, T. Wolf, A. A. Haghighirad, C. Meingast, A. J. Schofield, H. v. Löhneysen, Y. Matsuda, A. I. Coldea, and T. Shibauchi, Dichotomy Between the Hole and Electron Behavior in Multiband Superconductor FeSe Probed by Ultrahigh Magnetic Fields, Phys. Rev. Lett. **115**, 027006 (2015).

[27] D. Chareev, E. Osadchii, T. Kuzmicheva, J.-Y. Lin, S. Kuzmichev, O. Volkova, and A. Vasiliev, Single crystal growth and characterization of tetragonal FeSe$_{1-x}$ superconductors, CrystEngComm **15**, 1989 (2013).

[28] A. E. Böhmer, F. Hardy, F. Eilers, D. Ernst, P. Adelmann, P. Schweiss, T. Wolf, and C. Meingast, Lack of coupling between superconductivity and orthorhombic distortion in stoichiometric single-crystalline FeSe, Phys. Rev. B **87**, 180505(R) (2013).

[29] R. Willa, M. Fritz, and J. Schmalian, Strain tuning and anisotropic spin correlations in iron-based systems, Phys. Rev. B **100**, 085106 (2019).

[30] Cryostrain cell. Data sheet: CS100, Razorbill Instruments, 2019.

[31] J. Park, J. M. Bartlett, H. M. L. Noad, A. L. Stern, M. E. Barber, M. Kßnig, S. Hosoi, T. Shibauchi, A. P. Mackenzie, A. Steppke, and C. W. Hicks, Rigid platform for applying large tunable strains to mechanically delicate samples, Rev. Sci. Instrum. **91**, 083902 (2020).

[32] S.-H. Baek, D. V. Efremov, J. M. Ok, J. S. Kim, J. van den Brink, and B. Büchner, Nematicity and in-plane anisotropy of superconductivity in β-FeSe detected by ^{77}Se nuclear magnetic resonance, Phys. Rev. B **93**, 180502(R) (2016).

[33] A. E. Böhmer, V. Taufour, W. E. Straszheim, T. Wolf, and P. C. Canfield, Variation of transition temperatures and residual resistivity ratio in vapor-grown FeSe, Phys. Rev. B **94**, 024526 (2016).

[34] M. He, L. Wang, F. Hardy, L. Xu, T. Wolf, P. Adelmann, and C. Meingast, Evidence for short-range magnetic order in the nematic phase of FeSe from anisotropic in-plane magnetostriction and susceptibility measurements, Phys. Rev. B **97**, 104107 (2018).

[35] M. D. Watson, A. A. Haghighirad, L. C. Rhodes, M. Hoesch, and T. K. Kim, Electronic anisotropies revealed by detwinned angle-resolved photo-emission spectroscopy measurements of FeSe, New J. Phys. **19**, 103021 (2017).

[36] L. C. Rhodes, M. D. Watson, A. A. Haghighirad, D. V. Evtushinsky, and T. K. Kim, Revealing the single electron pocket of FeSe in a single orthorhombic domain, Phys. Rev. B **101**, 235128 (2020).

[37] F. Nabeshima, M. Kawai, T. Ishikawa, and A. Maeda, Systematic study on transport properties of FeSe thin films with various degrees of strain, Jpn. J. Appl. Phys. **57**, 120314 (2018).

[38] M. Bristow, P. Reiss, A. A. Haghighirad, Z. Zajicek, S. J. Singh, T. Wolf, D. Graf, W. Knafo, A. McCollam, and A. I. Coldea, Anomalous high-magnetic field electronic state of the nematic superconductors FeSe$_{1-x}$S$_x$, Phys. Rev. Res. **2**, 013309 (2020).

[39] M. Breitkreiz, P. M. R. Brydon, and C. Timm, Transport in multiband systems with hot spots on the fermi surface:

[40] Forward-scattering corrections, Phys. Rev. B **89**, 245106 (2014).

[41] L. Fanfarillo, E. Cappelluti, C. Castellani, and L. Benfatto, Unconventional Hall Effect in Pnictides from Interband Interactions, Phys. Rev. Lett. **109**, 096402 (2012).

[42] I. Paul and M. Garst, Lattice Effects on Nematic Quantum Criticality in Metals, Phys. Rev. Lett. **118**, 227601 (2017).

[43] P. Reiss, D. Graf, A. A. Haghighirad, W. Knafo, L. Drigo, M. Bristow, A. J. Schofield, and A. I. Coldea, Quenched nematic criticality separating two superconducting domes in an iron-based superconductor under pressure, Nat. Phys. **16**, 89 (2020).

[44] D. Labat and I. Paul, Pairing instability near a lattice-influenced nematic quantum critical point, Phys. Rev. B **96**, 195146 (2017).

[45] P. Blaha, K. Schwarz, F. Tran, R. Laskowski, G. K. H. Madsen, and L. D. Marks, WIEN2k: An APW+lo program for calculating the properties of solids, J. Chem. Phys. **152**, 074101 (2020).

[46] G. N. Phan, K. Nakayama, K. Sugawara, T. Sato, T. Urata, Y. Tanabe, K. Tanigaki, F. Nabeshima, Y. Imai, A. Maeda, and T. Takahashi, Effects of strain on the electronic structure, superconductivity, and nematicity in FeSe studied by angle-resolved photoemission spectroscopy, Phys. Rev. B **95**, 224507 (2017).

[47] C. Cai, T. T. Han, Z. G. Wang, L. Chen, Y. D. Wang, Z. M. Xin, M. W. Ma, Y. Li, and Y. Zhang, Momentum-resolved measurement of electronic nematic susceptibility in the FeSe$_{0.9}$S$_{0.1}$ superconductor, Phys. Rev. B **101**, 180501(R) (2020).

[48] M. Vojta, Quantum phase transitions, Rep. Prog. Phys. **66**, 2069 (2003).

[49] Y. Xing, H.-M. Zhang, H.-L. Fu, H. Liu, Y. Sun, J.-P. Peng, F. Wang, X. Lin, X.-C. Ma, Q.-K. Xue, J. Wang, and X. C. Xie, Quantum Griffiths singularity of superconductor-metal transition in Ga thin films, Science **350**, 542 (2015).

[50] P. Reiss, D. Graf, A. A. Haghighirad, T. Vojta, and A. I. Coldea, Signatures of a quantum Griffiths phase close to an electronic nematic quantum phase transition, arXiv:2103.07991.

[51] G. N. Phan, K. Nakayama, S. Kanayama, M. Kuno, K. Sugawara, T. Sato, and T. Takahashi, High-temperature superconductivity and lattice relaxation in lithium-deposited FeSe on SrTiO$_3$, J. Phys. Soc. Jpn. **86**, 033706 (2017).

[52] T. Terashima, N. Kikugawa, A. Kiswandhi, D. Graf, E.-S. Choi, J. S. Brooks, S. Kasahara, T. Watashige, Y. Matsuda, T. Shibauchi, T. Wolf, A. E. Böhmer, F. Hardy, C. Meingast, H. v. Löhneysen, and S. Uji, Fermi surface reconstruction in FeSe under high pressure, Phys. Rev. B **93**, 094505 (2016).

[52] https://doi.org/10.5281/zenodo.22558

[53] C. W. Hicks, M. E. Barber, S. D. Edkins, D. O. Brodsky, and A. P. Mackenzie, Piezoelectric-based apparatus for strain tuning, Rev. Sci. Instrum. **85**, 065003 (2014).

[54] J. P. Perdew, K. Burke, and M. Ernzerhof, Generalized Gradient Approximation Made Simple, Phys. Rev. Lett. **77**, 3865 (1996).

[55] J. M. Bartlett, A. Steppke, S. Hosoi, H. Noad, J. Park, C. Timm, T. Shibauchi, A. P. Mackenzie, and C. W. Hicks, Relationship between Transport Anisotropy and Nematicity in FeSe, Phys. Rev. X **11**, 021038 (2021).